Electronic supplementary information *for* Flow and deformation characteristics of a flexible microfluidic channel with axial gradients in wall elasticity

Pratyaksh Karan[‡a], Sankha Shuvra Das[‡a], Rabibrata Mukherjee[b], Jeevanjyoti Chakraborty[*a], Suman Chakraborty[*a]

‡ Authors have contributed equally.
* communicating authors: jeevan@mech.iitkgp.ac.in, suman@mech.iitkgp.ac.in
[a] *Department of Mechanical Engineering, Indian Institute of Technology, Kharagpur, India 721302.*
[b] *Department of Chemical Engineering, Indian Institute of Technology, Kharagpur, India 721302.*

Table S1 Characteristic scales of system physical variables

Physical variable	Characteristic Scale
r^*	$a = \varepsilon L$
z^*	L
$\bar{r}^*$	$A = \gamma L$
v_r^*	$\dfrac{Q}{\pi\varepsilon L^2}$
v_z^*	$\dfrac{Q}{\text{Area}_{\text{in}}} = \dfrac{Q}{\pi\varepsilon^2 L^2}$
p_f^*	$\dfrac{\mu Q}{\pi\varepsilon^4 L^3}$
p_w^*	$\dfrac{\mu Q}{\pi\varepsilon^4 L^3} + p_0^* = \dfrac{\mu Q(1+p_0)}{\pi\varepsilon^4 L^3}$
$u_{\bar{r}}^*, u_z^*$	$\theta a = \theta\varepsilon L$

S1 Governing Equations and Boundary Conditions

We discuss the flow modelling first. We consider a constant density Newtonian fluid undergoing steady fully-developed flow. With these assumptions, the governing equations for the flow dynamics are,

$$\frac{\partial v_r^*}{\partial r^*} + \frac{v_r^*}{r^*} + \frac{\partial v_z^*}{\partial z^*} = 0, \tag{S1}$$

$$0 = -\frac{1}{\mu}\frac{\partial p_f^*}{\partial r^*} + \frac{\partial^2 v_r^*}{\partial r^{*2}} + \frac{1}{r^*}\frac{\partial v_r^*}{r^*} - \frac{v_r^*}{r^{*2}} + \frac{\partial^2 v_r^*}{\partial z^{*2}}, \tag{S2}$$

$$0 = -\frac{1}{\mu}\frac{\partial p_f^*}{\partial z^*} + \frac{\partial^2 v_z^*}{\partial r^{*2}} + \frac{1}{r^*}\frac{\partial v_z^*}{r^*} + \frac{\partial^2 v_z^*}{\partial z^{*2}}. \tag{S3}$$

We non-dimensionalized the governing equations as per the scales presented in table S1. Retaining only leading ordered terms, the governing equations are,

$$\frac{\partial v_r}{\partial r} + \frac{v_r}{r} + \frac{\partial v_z}{\partial z} = 0, \tag{S4}$$

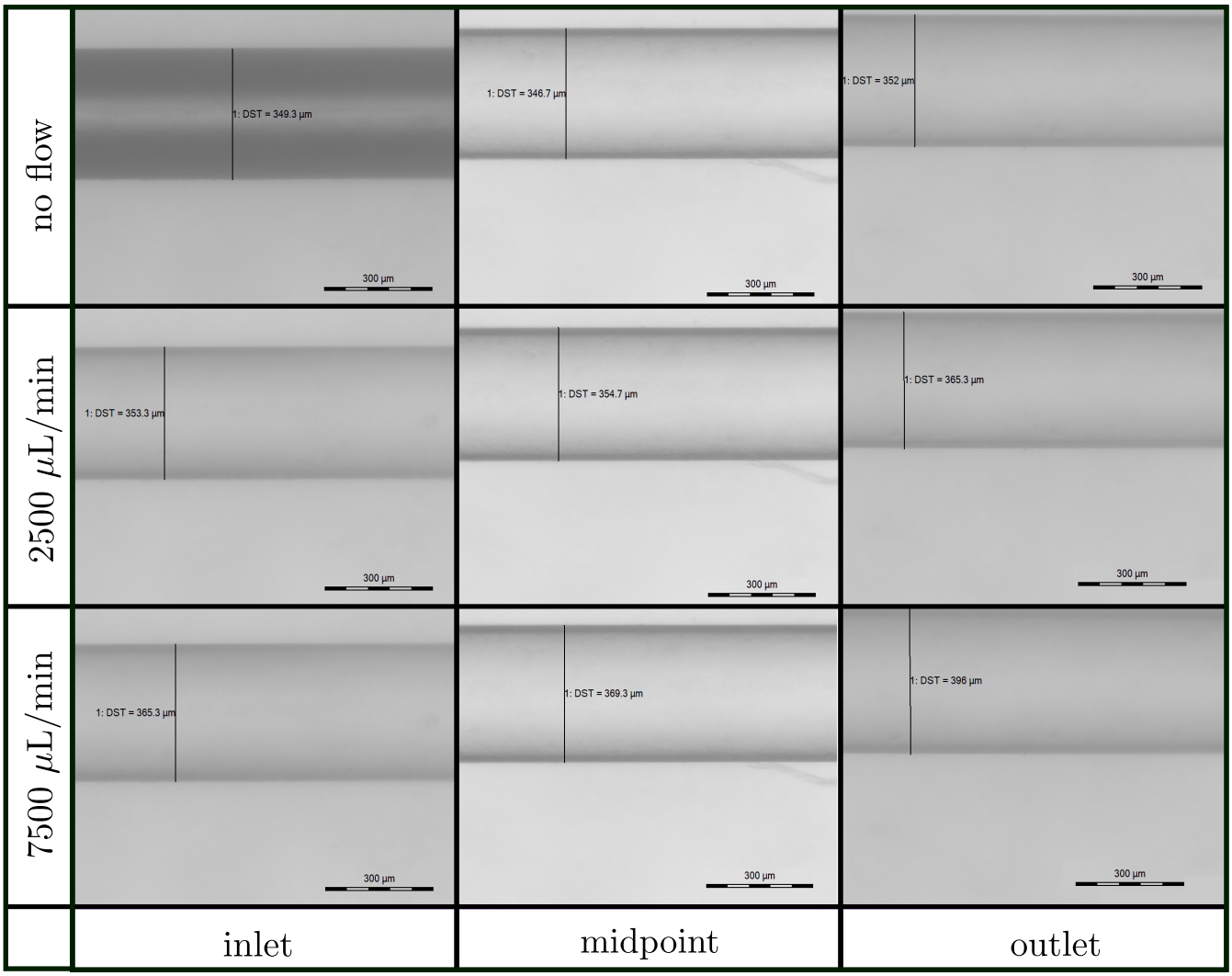

Fig. S1 Photographs of SmG channel profile at inlet (left), midpoint (center) and outlet (right) at flow-rates of zero (top), 2500 μL/min (mid) and 7500 μL/min (bottom).

$$0 = \frac{\partial p_f}{\partial r}, \tag{S5}$$

$$0 = -\frac{\partial p_f}{\partial z} + \frac{\partial^2 v_z}{\partial r^2}. \tag{S6}$$

These equations are subject to the boundary conditions,

$$p = 0, \text{ at } z = 1, \tag{S7}$$

$$v_r = v_z = 0, \text{ at } r = 1 + \theta\Delta, \tag{S8}$$

Solving equations (S4) to (S6) following procedure similar to that for Poiseuille flow, the solution for v_z is,

$$v_z = \frac{1}{4}\frac{dp_f}{dz}\left[(1+\theta\Delta)^2 - r^2\right]. \tag{S9}$$

To get the equation for pressure, we invoke the condition of flow rate being constant across different cross sections, i.e.,

$$Q = \int_0^{a+\Delta^*} 2\pi r^* v_z^* dr^* \implies 1 = 2\int_0^{1+\theta\Delta} v_z r dr. \tag{S10}$$

Subsequent algebra yields equation (1) in the main document, which is subjected to boundary condition S7 (re-iterated as equation (3) in the main document).

For the substrate deformation, the governing equation is the mechanical equilibrium equation, given as,

$$\bar{\nabla}^* \cdot \underline{\underline{\sigma}}^* = 0, \tag{S11}$$

where the Cauchy-Green stress tensor, $\underline{\underline{\sigma}}^*$ is,

$$\underline{\underline{\sigma}}^* = \lambda \,\mathrm{tr}\left(\underline{\underline{E}}^*\right) + 2G\underline{\underline{E}}^*, \tag{S12}$$

and, $\underline{\underline{E}}^*$ is the infinitesimal strain tensor, given as,

$$\underline{\underline{E}}^* = \frac{1}{2}\left[\nabla^*\vec{u}^* + (\nabla^*\vec{u}^*)^T\right], \tag{S13}$$

and $\bar{\nabla}^*$ is the gradient operator in the cylindrical co-ordinate system $\bar{r}^*$-z^*-ϕ [1], with axisymmetry, i.e. $\dfrac{\partial}{\partial\phi} \equiv 0$, and zero ϕ-component, i.e. $\Gamma_\phi = 0$ for any general vector $\vec{\Gamma}$.

Plugging equation (S13) into equation (S12) and then equation (S12) into equation (S11) yields the two equations that are the $\bar{r}^*$-deformation and the z^*-deformation governing equations. These equations are then non-dimensionalized with the scales given in S1, giving us,

$$\left(2+\frac{\lambda}{G}\right)\left(\frac{\partial^2 u_{\bar{r}}}{\partial \bar{r}^2} + \frac{1}{\bar{r}}\frac{\partial u_{\bar{r}}}{\partial \bar{r}} - \frac{u_{\bar{r}}}{\bar{r}^2}\right) + \gamma\left(1+\frac{\lambda}{G}\right)\frac{\partial^2 u_z}{\partial \bar{r}\partial z} + \gamma^2\frac{\partial^2 u_{\bar{r}}}{\partial z^2} = 0, \tag{S14}$$

$$\frac{\partial^2 u_{\bar{z}}}{\partial \bar{r}^2} + \frac{1}{\bar{r}}\frac{\partial u_{\bar{z}}}{\partial \bar{r}} + \gamma\left(1+\frac{\lambda}{G}\right)\left(\frac{\partial^2 u_{\bar{r}}}{\partial \bar{r}\partial z} + \frac{1}{\bar{r}}\frac{\partial u_{\bar{r}}}{\partial z}\right) + \gamma^2\left(2+\frac{\lambda}{G}\right)\frac{\partial^2 u_{\bar{r}}}{\partial z^2} = 0, \tag{S15}$$

Equations (S14) and (S15) are subjected to the traction balance boundary conditions at the channel wall, non-dimensionalized versions of which are,

$$\frac{\partial u_{\bar{r}}}{\partial \bar{r}} + \left(\frac{\lambda}{\lambda+G}\right)\left(\frac{u_{\bar{r}}}{\bar{r}} + \gamma\frac{\partial u_z}{\partial z}\right) - \theta\varepsilon\left(\frac{G}{\lambda+2G}\right)\left(\gamma\frac{\partial u_{\bar{r}}}{\partial z} + \frac{\partial u_z}{\partial \bar{r}}\right)\frac{\partial u_{\bar{r}}}{\partial z} =$$
$$-\frac{\gamma\mu Q}{\pi\theta\varepsilon^5 L^3(\lambda+2G)}\left[(1+p_0)p_w - \varepsilon^2\frac{\partial v_r}{\partial r} + \varepsilon^2\theta\left(\frac{\partial v_z}{\partial r} + \varepsilon^2\frac{\partial v_r}{\partial z}\right)\frac{\partial u_{\bar{r}}}{\partial z}\right]$$
$$\approx -\frac{\gamma\mu Q(1+p_0)p_w}{\pi\theta\varepsilon^5 L^3(\lambda+2G)}, \quad \text{(S16)}$$

$$\frac{\partial u_{\bar{z}}}{\partial \bar{r}} + \gamma\frac{\partial u_{\bar{r}}}{\partial z} - \theta\gamma\varepsilon\left(2+\frac{\lambda}{G}\right)\frac{\partial u_z}{\partial z}\frac{\partial u_{\bar{r}}}{\partial z} - \theta\varepsilon\frac{\lambda}{G}\left(\frac{\partial u_{\bar{r}}}{\partial \bar{r}} + \frac{u_{\bar{r}}}{\bar{r}}\right) =$$
$$-\varepsilon\cdot\frac{\gamma\mu Q}{\pi\theta\varepsilon^5 L^3 G}\left[\frac{\partial v_z}{\partial r} + \varepsilon^2\frac{\partial v_r}{\partial z} + \theta\left((1+p_0)p_w - \varepsilon^2\frac{\partial v_z}{\partial z}\right)\frac{\partial u_{\bar{r}}}{\partial z}\right]$$
$$\approx \varepsilon\cdot\frac{\gamma\mu Q(1+p_0)p_w}{\pi\theta\varepsilon^5 L^3 G}\frac{\partial v_z}{\partial r}, \quad \text{(S17)}$$

at $\bar{r} = \dfrac{\varepsilon}{\gamma}$, and the far-end zero-displacement condition, i.e.,

$$u_{\bar{r}} = u_z = 0 \text{ at } \bar{r} = 1. \quad \text{(S18)}$$

For the setup that we are studying, the channel is significantly longer than its radius. Therefore, we consider the depth of deformation, A to be much smaller than L, i.e. $\gamma \ll 1$. Equations (S14) to (S17) thus simplify to,

$$\frac{\partial^2 u_{\bar{r}}}{\partial \bar{r}^2} + \frac{1}{\bar{r}}\frac{\partial u_{\bar{r}}}{\partial \bar{r}} - \frac{u_{\bar{r}}}{\bar{r}^2} = 0, \quad \text{(S19)}$$

$$\frac{\partial^2 u_{\bar{z}}}{\partial \bar{r}^2} + \frac{1}{\bar{r}}\frac{\partial u_{\bar{z}}}{\partial \bar{r}} = 0, \quad \text{(S20)}$$

$$\frac{\partial u_{\bar{r}}}{\partial \bar{r}} + \left(\frac{\lambda}{\lambda+G}\right)\left(\frac{u_{\bar{r}}}{\bar{r}} + \gamma\frac{\partial u_z}{\partial z}\right) = -\frac{\gamma\mu Q(1+p_0)p_w}{\pi\theta\varepsilon^5 L^3(\lambda+2G)}, \quad \text{(S21)}$$

$$\frac{\partial u_{\bar{z}}}{\partial \bar{r}} = \varepsilon\cdot\frac{\gamma\mu Q(1+p_0)p_w}{\pi\theta\varepsilon^5 L^3 G}\frac{\partial v_z}{\partial r}. \quad \text{(S22)}$$

Equations (S19) and boundary condition (S21) indicate that $\bar{r}$-deformation is de-coupled from z-deformation and is analytically solvable. Furthermore, since the substrate deformation is dominant in the radial direction and is caused by fluid pressure, the LHS and RHS of equation (S21), which signify the force at the channel wall from the fluid and solid sides, should scale equal. This gives the expression for θ as presented in equation (7) in the main document. The solution for $u_{\bar{r}}$ is obtained

as,

$$u_{\bar{r}} = \frac{\varepsilon^2}{2\gamma^2}\left[1+\left(1+\frac{\lambda}{G}\right)\frac{\varepsilon^2}{\gamma^2}\right]^{-1}\left[\frac{1}{\bar{r}}-\bar{r}\right]\left(\frac{\lambda_0+2G_0}{G}\right)p_w, \tag{S23}$$

Substituting $\bar{r} = \dfrac{\varepsilon}{\gamma}$ in equation (S23) gives the expression for deflection Δ as,

$$\Delta = \frac{\varepsilon}{2\gamma}\left[1+\left(1+\frac{\lambda}{G}\right)\frac{\varepsilon^2}{\gamma^2}\right]^{-1}\left[1-\frac{\varepsilon^2}{\gamma^2}\right]\left(\frac{\lambda_0+2G_0}{G}\right)p_w. \tag{S24}$$

Furthermore, for the setup we are studying, the substrate thickness, $R-a$, is much larger than the channel undeformed radius, a. As a result, the substrate can be approximated as an infinite medium in comparison to the channel radius, i.e. $A \gg a \implies \gamma \gg \varepsilon$. Hence, equations (S23) and (S24) can be approximated as,

$$u_{\bar{r}} = \frac{\varepsilon^2(\lambda_0+2G_0)}{2\gamma^2 G}\left[\frac{1}{\bar{r}}-\bar{r}\right]p_w, \tag{S25}$$

$$\Delta = \frac{\varepsilon(\lambda_0+2G_0)}{2\gamma G}p_w. \tag{S26}$$

which is re-iterated in the main text as equation 2 in the main document.
Summarily, in our theoretical analysis, we have assumed fully-developed flow in the channel and $\varepsilon \ll \gamma \ll 1$ to simplify and solve the governing equations and boundary conditions.

S2 Newton-Raphson Method to Compute the Analytical Solution for p_w and Δ

Equations (1), (3) and (2) in the main document are coupled and are solved using a Newton-Raphson root-finding method. For employing this method, the equations are first discretized using a finite-difference scheme. The z-axis is uniformly divided into n points. The discretized versions of equations (1), (3) and (2) are,

$$(1+\theta\Delta_i)^4\left.\frac{\partial p_w}{\partial x}\right|_i + \frac{8}{1+p_0} = 0 \text{ for } i = 1:n-1 \tag{S27}$$

$$p_w = \frac{p_0}{1+p_0} \text{ for } i = n \tag{S28}$$

$$\Delta_i = K_i p_{w,i} \text{ for } i = 1:n \tag{S29}$$

The multi-variable Newton-Raphson method for solving non-linear system of algebraic equation employs a Jacobian matrix J and a residual array R. For equations (S27) to (S29) that have $2n$ unknowns (n discrete values of p_w and n discrete values of Δ), J is a $2n \times 2n$ matrix and R is a $2n$ array. The non-zero entries of R and J are presented in the following equations.

$$R_i = (1+\theta\Delta_i)^4\left.\frac{\partial p_w}{\partial x}\right|_i^{FD} + \frac{8}{1+p_0} = 0 \text{ for } i = 1 \tag{S30}$$

$$R_i = (1+\theta\Delta_i)^4\left.\frac{\partial p_w}{\partial x}\right|_i^{CD} + \frac{8}{1+p_0} = 0 \text{ for } i = 2:n-1 \tag{S31}$$

$$J_{1,1} = -\frac{3(1+\theta\Delta_1)^4}{2dr},\ J_{1,2} = \frac{2(1+\theta\Delta_1)^4}{dr},\ J_{1,3} = -\frac{(1+\theta\Delta_1)^4}{2dr} \tag{S32}$$

$$J_{i,i-1} = -\frac{(1+\theta\Delta_1)^4}{2dr},\ J_{i,i+1} = \frac{(1+\theta\Delta_1)^4}{2dr} \text{ for } i = 2:n-1 \tag{S33}$$

$$J_{1,1+n} = 4\theta(1+\theta\Delta_1)^3 \left.\frac{\partial p_w}{\partial x}\right|_1^{FD} \tag{S34}$$

$$J_{i,i+n} = 4\theta(1+\theta\Delta_i)^3 \left.\frac{\partial p_w}{\partial x}\right|_i^{FD} \text{ for } i = 2:n-1 \tag{S35}$$

$$R_n = p_{w,n} - \frac{p_0}{1+p_0} \tag{S36}$$

$$J_{n,n} = 1 \tag{S37}$$

$$R_{n+i} = \Delta_i - K_i p_{w,i} \text{ for } i = 1:n \tag{S38}$$

$$J_{n+i,n+i} = 1 \text{ for } i = 1:n \tag{S39}$$

$$J_{n+i,i} = -K_i \text{ for } i = 1:n \tag{S40}$$

The solution for p_w and Δ are obtained by iterating over,

$$p_{w,i} = p_{w,i} - \left(J^{-1}R\right)_i, \tag{S41}$$

$$\Delta_i = \Delta_i - \left(J^{-1}R\right)_{n+i}, \tag{S42}$$

till $||R||$ is smaller than a prescribed tolerance.

S3 Young's modulus characterization of PDMS samples

For the theoretical computations, we require the Young's modulus and Poisson's ratio of the substrate material. Since PDMS is nearly-incompressible, we take the Poisson's ratio to be 0.49 for the theoretical computations (the analytical scheme does not allow for Poisson's ratio to be taken as exactly 0.5 because the value of λ for $\nu = 0.5$ is ∞). For the Young's modulus, we conduct extensional testing of slender samples of cross-section 1.5 mm $\times$ 4.5 mm and length 10 mm cut out from six equally-spaced locations in the SmG setup. Each sample is stretched uniaxially and the force and extension measurements give the Young's modulus of the sample. Since we assume the cross-linking ratio to vary linearly along the channel length for SmG, the obtained Young's modulus for the six samples gives us six data points for the variation of Young's modulus with cross-linking ratio. We fit a power-law variation of the form,

$$E_y = E_0 c^{-n} \tag{S43}$$

on this data set. E_y is the Young's modulus and c is the cross-linking ratio. The values of E_0 and n are obtained as 410 MPa and 2.235 respectively. We present the data points, the variation as per equation (S43), and three sets of variation of Young's modulus with cross-linking ratio as presented by Wang *et al.*[2] in figure S2.

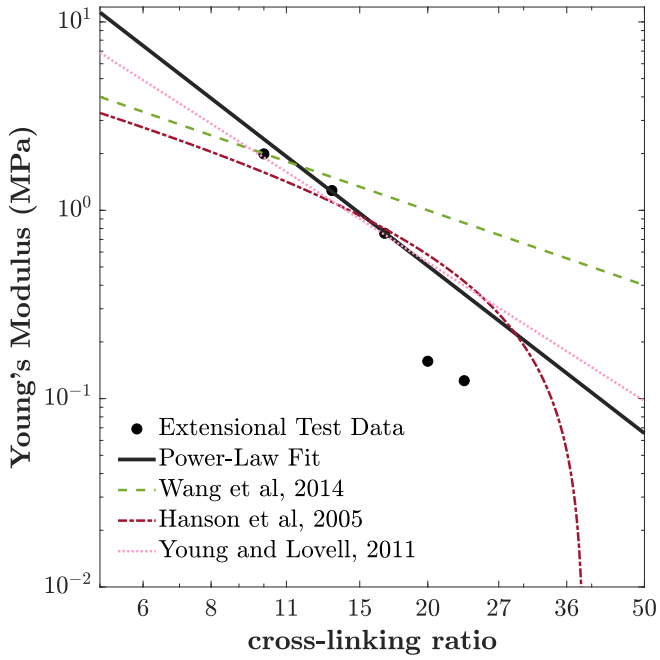

Fig. S2 Young's modulus variation with cross-linking ratio as per the power-Law fit in equation (S43) (solid black line), as obtained for the five samples in extensional test (black circle markers), as obtained in compression measurements by Wang *et al.*[2] (green dashed line), as obtained in tension measurements by Hanson *et al.*[3] and presented in Wang *et al.*[2] (dashed-dot maroon line), and as obtained in compression measurements by Young and Lovell[4] and presented in Wang *et al.*[2] (dotted pink line); the plot is logarithmic-scaled in both axes

S4 Theoretical analysis of the four cases - SmG, StG, SHS and HSH

The different aspects of flow and deformation in a soft microchannel can have distinctive implications depending on the specific application on hand. A possible application is shape control of microchannels, which is useful in studying rheology and species transport[5–13], demanding commensurate understanding of the deformation and flow. Other future scopes of microchannel elastohydrodynamics include its coupling with additional physical effects like electrokinetics, hydrophobicity and deviation from continuum[14–20]. Keeping these aspects in view, we analyse here the essential physical perspectives of elastohydrodynamics of the four setups studied in this work - SmG, StG, SHS and HSH, as obtained from our theoretical analysis.

We discuss SmG first. The trends for different system variables are presented in figure S3. In figure S3a, the variations of cross linking ratio and Young's modulus along the channel length are presented. The cross-linking ratio varies linearly from inlet to outlet as a result of significant diffusion due to slow solidification in ambient temperature. Variation of Young's modulus with cross-linking ratio is discussed in section S3. Variation of pressure gauged with atmospheric (i.e. variation of p_w^*) along channel length for the different flow rates is presented in figure S3b. As expected, pressure is higher for higher flow rates. The pressure profile can be seen to deviate slightly from linear, with the derivation being higher for higher flow rates. This is the outcome of wall deflection, which results in different radius at different cross-sections. The outlet pressure (i.e. p_w^* at $z^* = 5$ cm) is higher for higher flow rates, and exhibits a linear variation with flow rate. The outlet pressure (and thus the

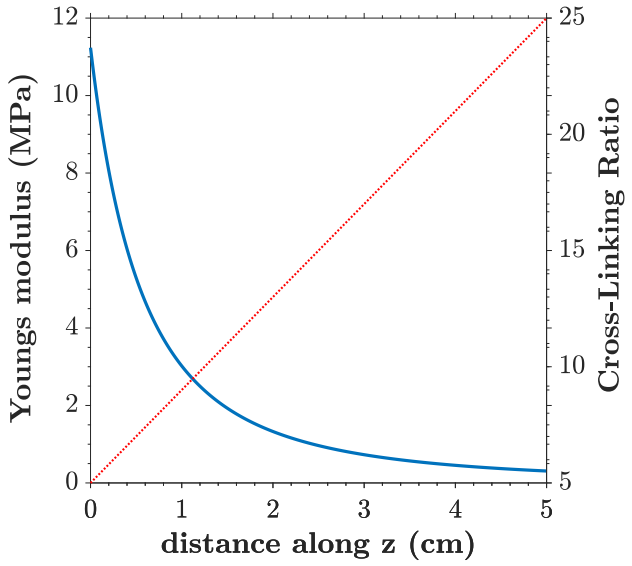
Youngs modulus (MPa)
Cross-Linking Ratio
distance along z (cm)
0
2
4
6
8
10
12
5
10
15
20
25
0
1
2
3
4
5

(a)

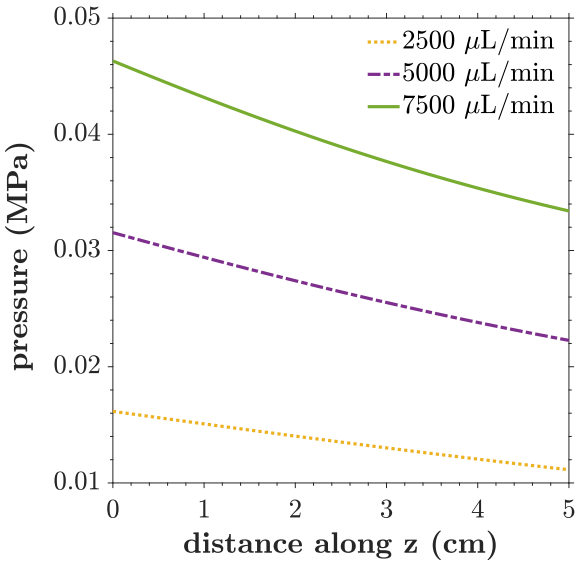
pressure (MPa)
distance along z (cm)
2500 μL/min
5000 μL/min
7500 μL/min
0.01
0.02
0.03
0.04
0.05
0
1
2
3
4
5

(b)

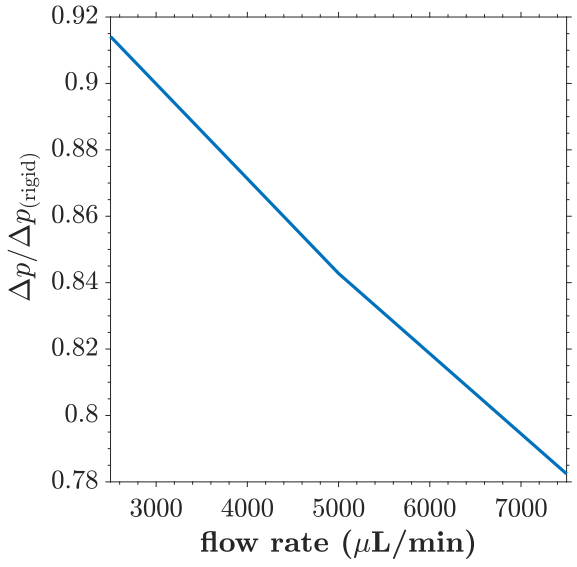
Δp/Δp(rigid)
flow rate (μL/min)
0.78
0.8
0.82
0.84
0.86
0.88
0.9
0.92
3000
4000
5000
6000
7000

(c)

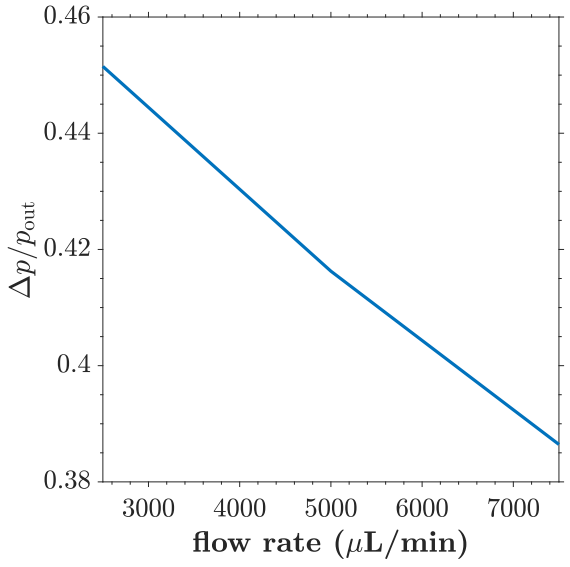
Δp/pout
flow rate (μL/min)
0.38
0.4
0.42
0.44
0.46
3000
4000
5000
6000
7000

(d)

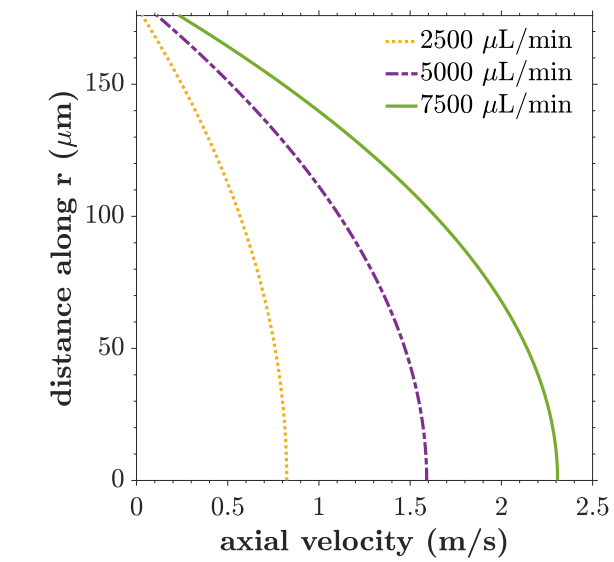

(e)

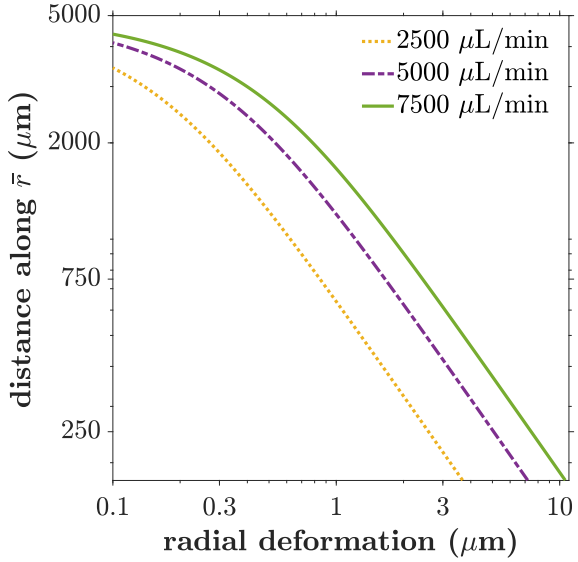

(f)

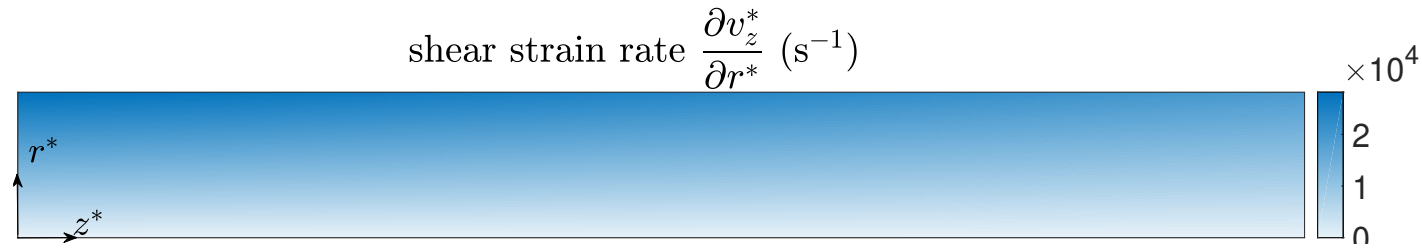

(g)

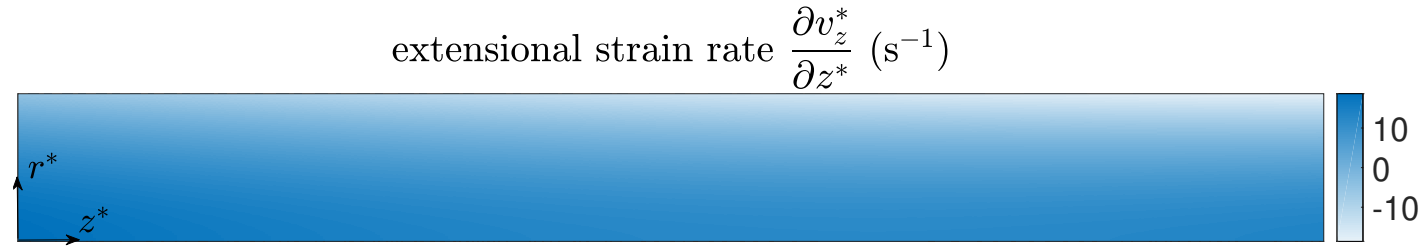

(h)

Fig. S3 For SmG, (a) axial variation of Young's modulus (solid blue line, left vertical axis) and cross-linking ratio (dotted red line, right vertical axis), (b) axial variation of pressure (gauged with atmospheric) for the different flow rates, (c) variation with flow rate of ratio of pressure drop over channel to the pressure drop over a counterpart rigid channel, (d) variation with flow rate of ratio of pressure drop over channel to outlet pressure gauged with atmospheric pressure, (e) profile of axial flow velocity in the channel along radial distance at the mid cross-section (i.e. at $z^* = 2.5$ cm), (f) profile of radial substrate deformation along radial distance at the mid cross-section (i.e. at $z^* = 2.5$ cm), (g) surface map of shear strain rate $\left(\frac{\partial v_z^*}{\partial r^*}\right)$ in the channel for the flow rate of 7500 μL/min, and (h) surface map of extensional strain rate $\left(\frac{\partial v_z^*}{\partial z^*}\right)$ in the channel for the flow rate of 7500 μL/min.

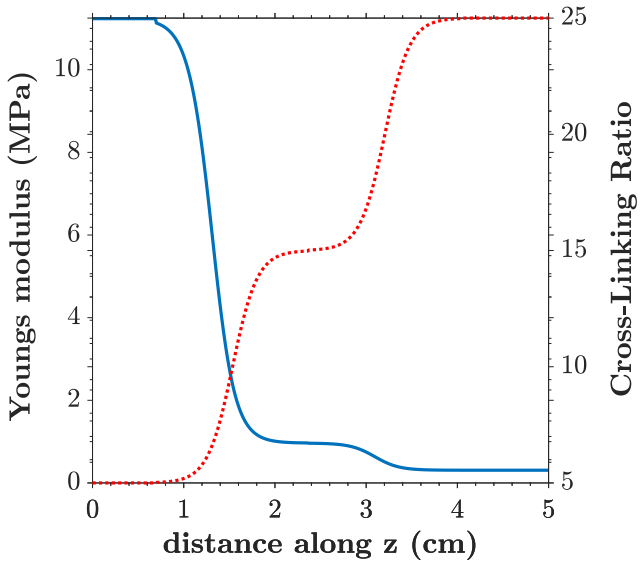
Youngs modulus (MPa)
Cross-Linking Ratio
distance along z (cm)
0
2
4
6
8
10
5
10
15
20
25
0
1
2
3
4
5

(a)

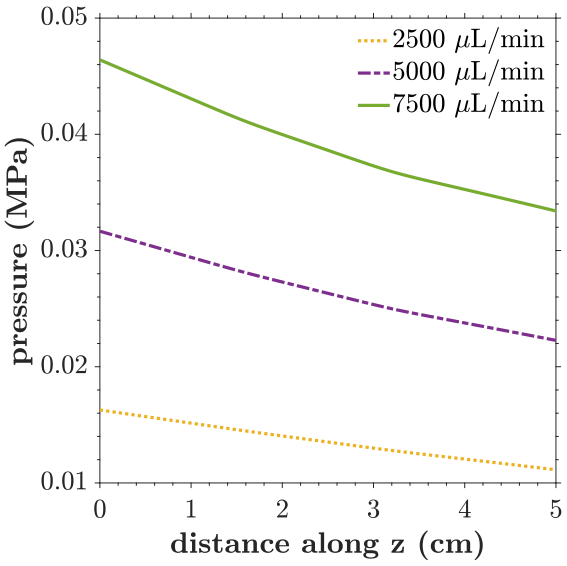
pressure (MPa)
distance along z (cm)
2500 μL/min
5000 μL/min
7500 μL/min
0.01
0.02
0.03
0.04
0.05
0
1
2
3
4
5

(b)

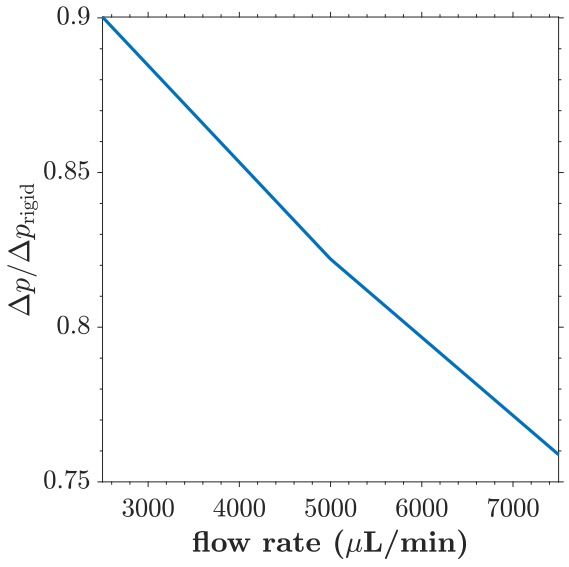
Δp/Δp_rigid
flow rate (μL/min)
0.75
0.8
0.85
0.9
3000
4000
5000
6000
7000

(c)

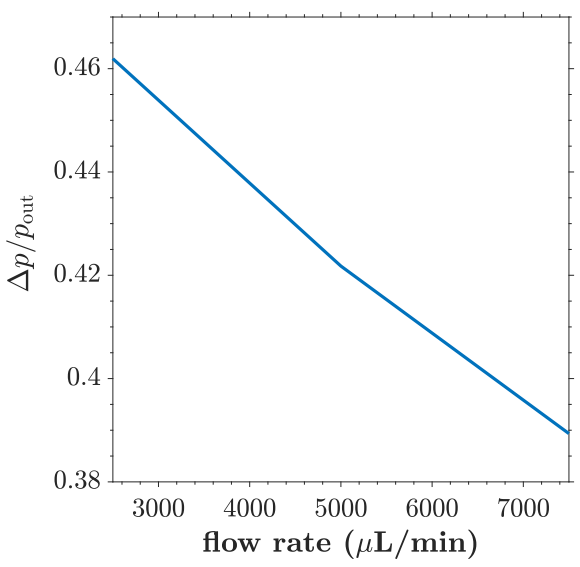
Δp/p_out
flow rate (μL/min)
0.38
0.4
0.42
0.44
0.46
3000
4000
5000
6000
7000

(d)

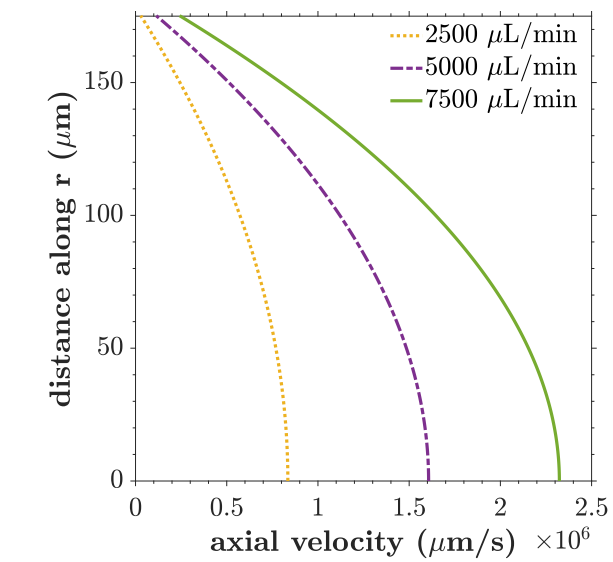

(e)

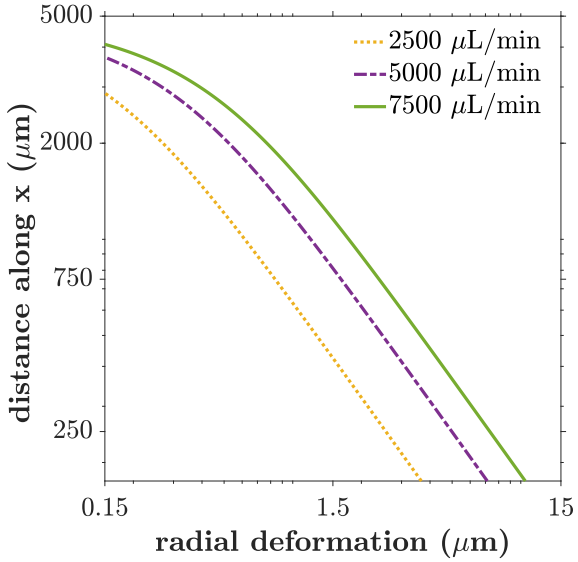

(f)

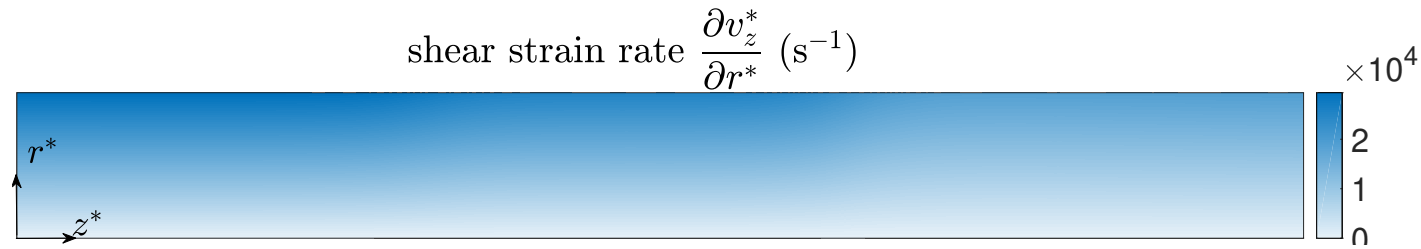

(g)

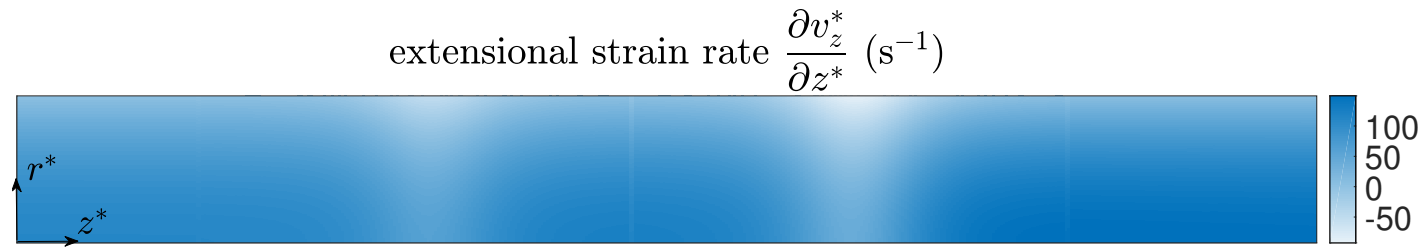

(h)

Fig. S4 For StG, (a) axial variation of Young's modulus (solid blue line, left vertical axis) and cross-linking ratio (dotted red line, right vertical axis), (b) axial variation of pressure (gauged with atmospheric) for the different flow rates, (c) variation with flow rate of ratio of pressure drop over channel to the pressure drop over a counterpart rigid channel, (d) variation with flow rate of ratio of pressure drop over channel to outlet pressure gauged with atmospheric pressure, (e) profile of axial flow velocity in the channel along radial distance at the mid cross-section (i.e. at $z^* = 2.5$ cm), (f) profile of radial substrate deformation along radial distance at the mid cross-section (i.e. at $z^* = 2.5$ cm), (g) surface map of shear strain rate $\left(\frac{\partial v_z^*}{\partial r^*}\right)$ in the channel for the flow rate of 7500 μL/min, and (h) surface map of extensional strain rate $\left(\frac{\partial v_z^*}{\partial z^*}\right)$ in the channel for the flow rate of 7500 μL/min.

pressure through the channel) is of the order of 10-100 kPa. In figure S3d, the pressure drop over the channel in comparison to the outlet pressure gauged with atmospheric (which is simply the pressure head due to the drainage tube) for different flow rates is presented. The values indicate that the pressure drop over the channel and pressure head due to drainage tube are of the same order. This implies that the drainage tube pressure head has significant contribution to the channel wall deflection. Also, while this ratio is expected to be constant for a rigid channel, the obtained ratio is smaller for higher flow rates, a consequence of channel deformation. Variation of the ratio of pressure drop over the channel to pressure drop over an analogous rigid channel with the three different flow rates is presented in figure S5c. This ratio is always smaller than unity, i.e., the pressure drop over the deformed channel is always lower than the rigid counterpart. Furthermore, this ratio is smaller for larger flow rate, an outcome of higher wall deflection at larger flow rate. In figure S3e, the velocity profile at the mid cross-section (i.e. at $z^* = 2.5$ cm) is presented. The velocities are of the order of 1 m/s. In figure S3f, the substrate deformation in the substrate bulk at $z^* = 2.5$ cm is presented. Both the axes are logarithmic-scaled. The deformation reduces to smaller than 1 μm for all flow rates at the radial distance of $\sim$0.2 cm, which is considerably less than the geometric bound of the fabricated micro-channels, $\sim$0.5 cm. At the radial distance of $\sim$0.5 cm, the radial deformation reduces to smaller than $\sim$0.1 μm. Hence, the assumption of infinitely-bound substrate for the current study's theoretical modelling can be deemed appropriate. In figures S3g and S3h, surface maps for shear strain rate and extensional strain rate in the microchannel are respectively presented. As expected, the shear strain rate varies from zero at the channel centreline to its maximum value at the channel wall, with the magnitude being $\sim 10^4$ s^{-1}. This amounts to shear stress of magnitude $\sim$10 Pa at the channel wall. In comparison, the extensional strain rate is much lower at $\sim 10^1$ s^{-1}.

We discuss StG next, presented in figure S4. In figure S4a, the variation of cross linking ratio can be seen to be stepped along the channel length, the result of arrested diffusion due to quick solidification at elevated temperature. Resultantly, the Young's modulus is also stepped. The range of cross-linking ratio and Young's modulus is however same as that for SmG (figure S3a). The next six panels, i.e. figures S4b to S4g, are qualitatively same as and quantitatively approximate to their SmG counterparts, figures S3b to S3g respectively. However, in figure S4h, we observe the effect of the stepped nature of channel wall deflection, which leads the extensional strain rate to exhibit higher positive as well as negative magnitudes and sharper variations at the location of the steps.

The counterpart trends for SHS, presented in figure S5, are also similar to those for SmG, except for the figures S5a, S5g and S5h. In figure S5a, the cross-linking ratio has a dip at the channel centre, leading to a spike in Young's modulus there. The shear strain rate (figure S5g) is similar to that for SmG (figure S3g) and has similar magnitude. However, a fairly discernible patch is visible in the middle of the channel, where the shear strain rate is higher in magnitude than on either side. On the other hand, the extensional strain rate for SHS (figure S5h) can be seen to be an order of magnitude higher than SmG (figure S3h), as well as have a significantly different profile. More specifically, as the fluid flows from inlet to outlet, it undergoes significant extension followed by significant contraction at the two ends of the central thin strip.

Lastly, the trends for HSH, presented in figure S6, are also similar to those for SmG, except for the figures S6a, S6g and S6h. These three panels, i.e. figures S6a, S6g and S6h, are simply the converse of their counterparts for SHS, figures S5a, S5g and S5h respectively.

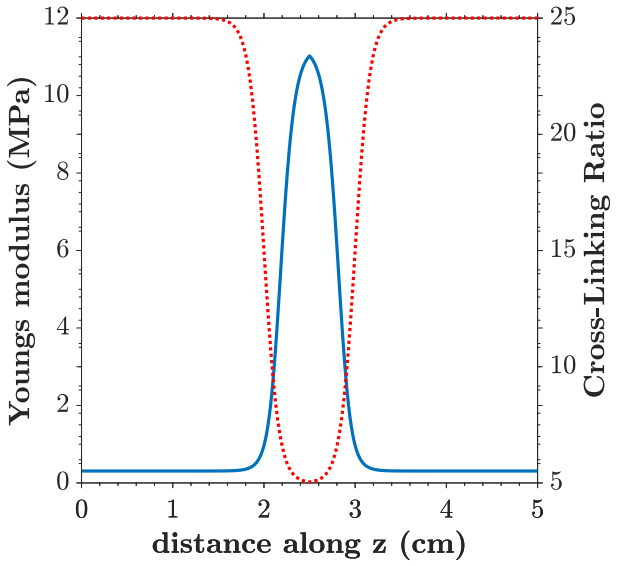
Youngs modulus (MPa)
Cross-Linking Ratio
distance along z (cm)

(a)

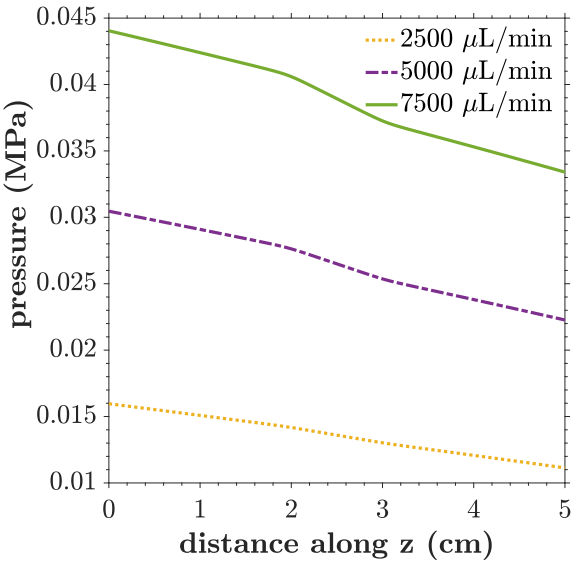
2500 μL/min
5000 μL/min
7500 μL/min
pressure (MPa)
distance along z (cm)

(b)

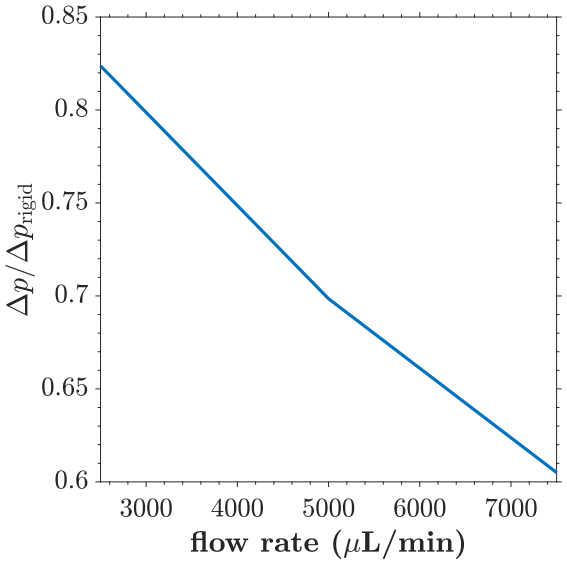
$\Delta p/\Delta p_{\text{rigid}}$
flow rate (μL/min)

(c)

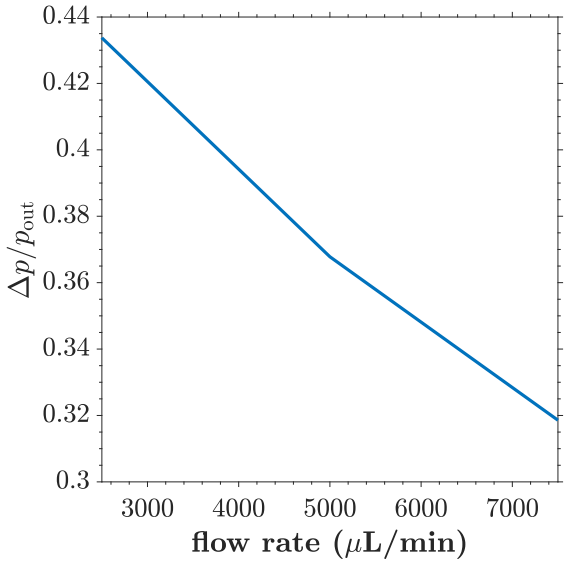
$\Delta p/p_{\text{out}}$
flow rate (μL/min)

(d)

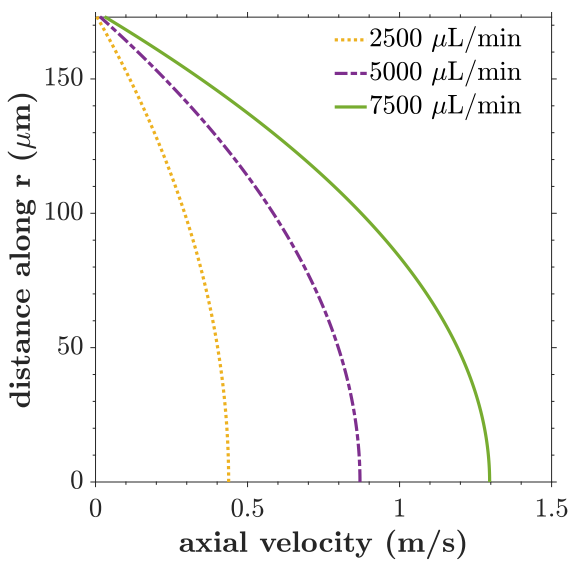

(e)

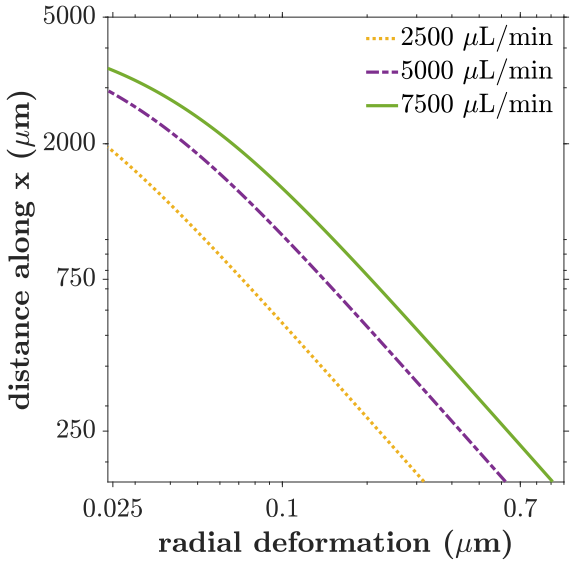

(f)

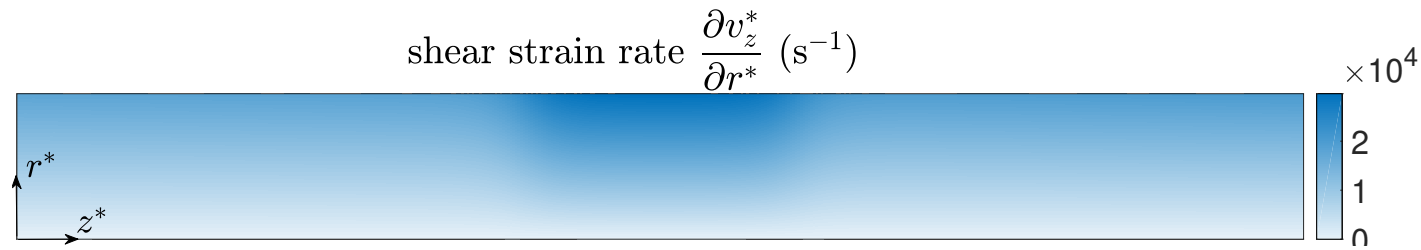

(g)

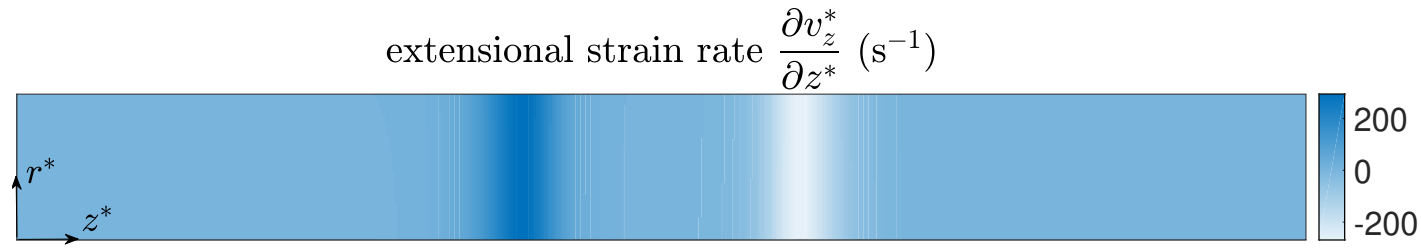

(h)

Fig. S5 For SHS, (a) axial variation of Young's modulus (solid blue line, left vertical axis) and cross-linking ratio (dotted red line, right vertical axis), (b) axial variation of pressure (gauged with atmospheric) for the different flow rates, (c) variation with flow rate of ratio of pressure drop over channel to the pressure drop over a counterpart rigid channel, (d) variation with flow rate of ratio of pressure drop over channel to outlet pressure gauged with atmospheric pressure, (e) profile of axial flow velocity in the channel along radial distance at the mid cross-section (i.e. at $z^* = 2.5$ cm), (f) profile of radial substrate deformation along radial distance at the mid cross-section (i.e. at $z^* = 2.5$ cm), (g) surface map of shear strain rate $\left(\frac{\partial v_z^*}{\partial r^*}\right)$ in the channel for the flow rate of 7500 μL/min, and (h) surface map of extensional strain rate $\left(\frac{\partial v_z^*}{\partial z^*}\right)$ in the channel for the flow rate of 7500 μL/min.

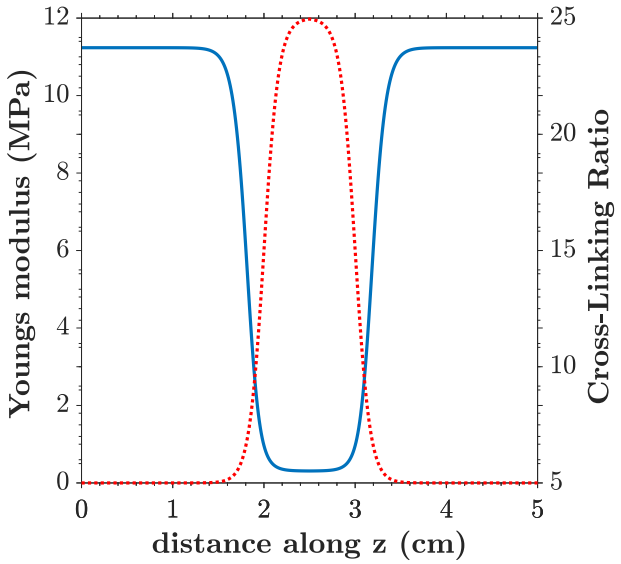
Youngs modulus (MPa)
Cross-Linking Ratio
distance along z (cm)

(a)

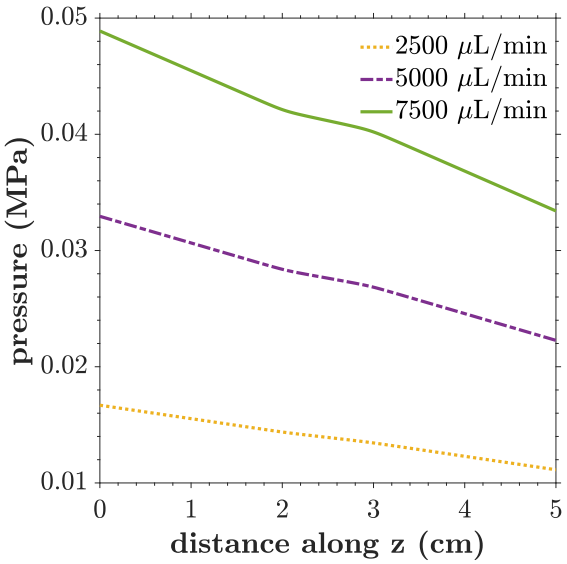
2500 μL/min
5000 μL/min
7500 μL/min
pressure (MPa)
distance along z (cm)

(b)

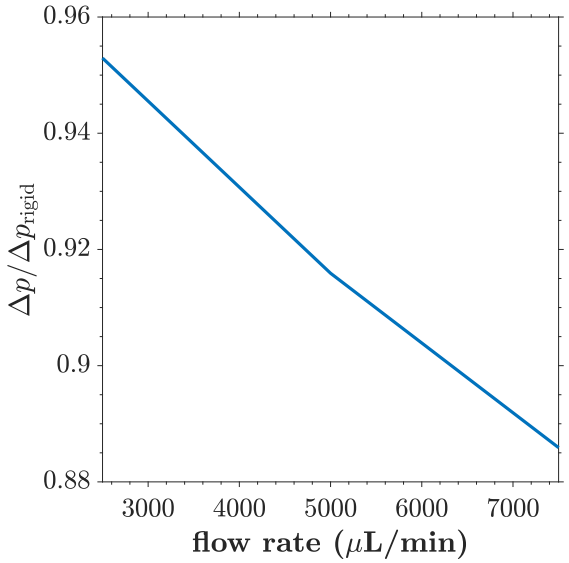
$\Delta p/\Delta p_{\text{rigid}}$
flow rate (μL/min)

(c)

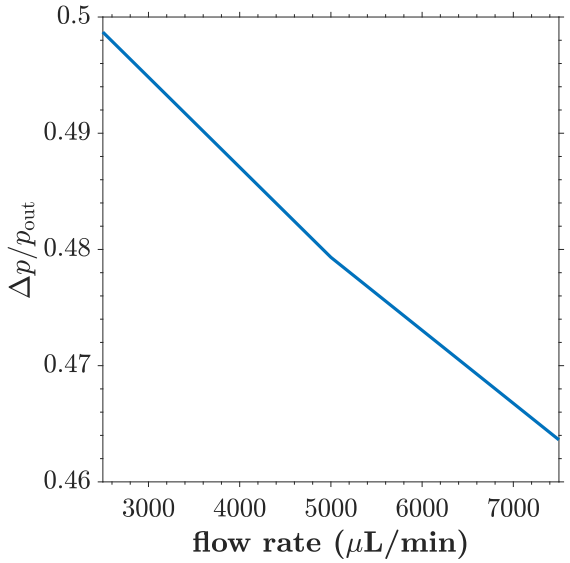
$\Delta p/p_{\text{out}}$
flow rate (μL/min)

(d)

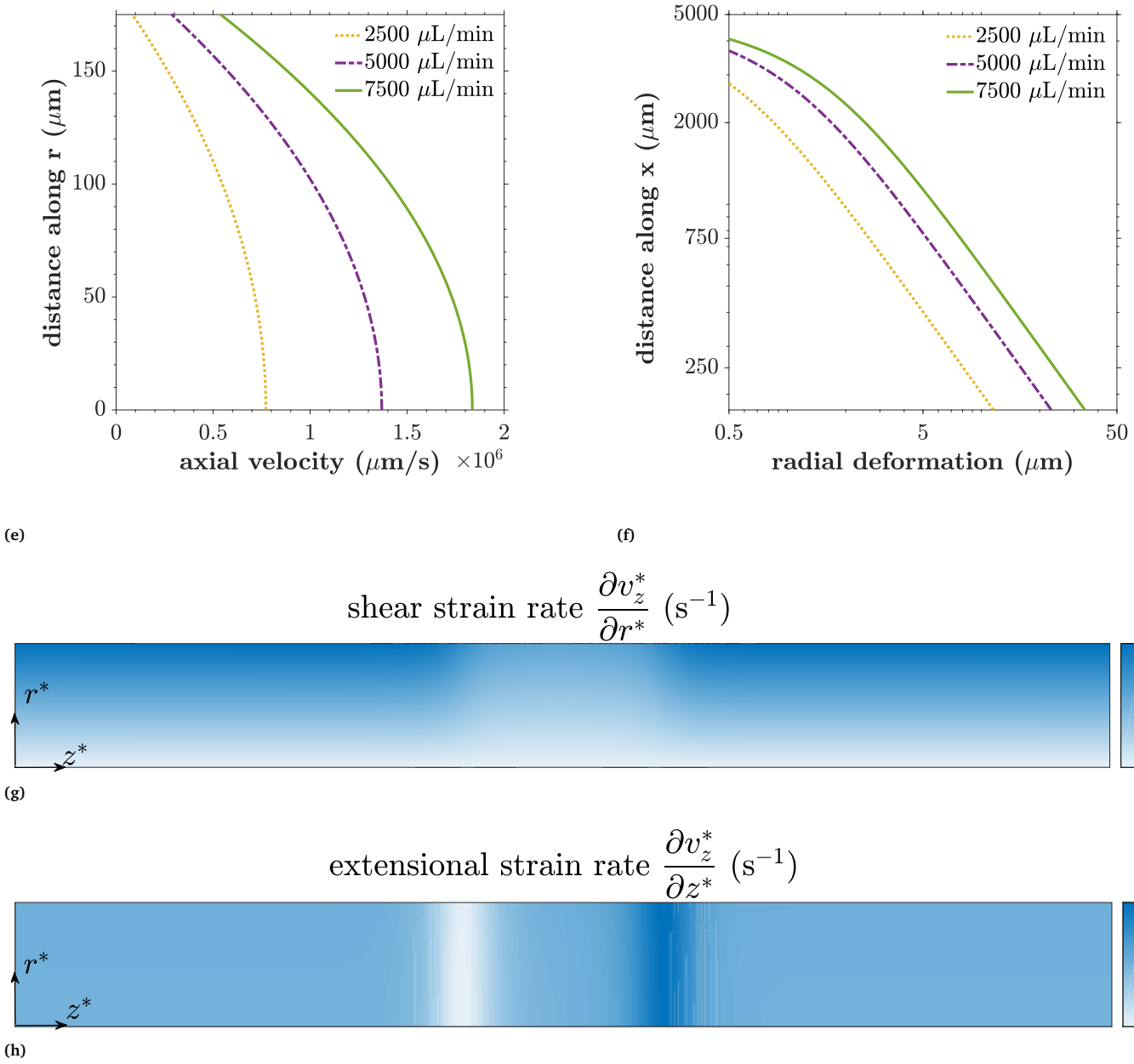

Fig. S6 For HSH, (a) axial variation of Young's modulus (solid blue line, left vertical axis) and cross-linking ratio (dotted red line, right vertical axis), (b) axial variation of pressure (gauged with atmospheric) for the different flow rates, (c) variation with flow rate of ratio of pressure drop over channel to the pressure drop over a counterpart rigid channel, (d) variation with flow rate of ratio of pressure drop over channel to outlet pressure gauged with atmospheric pressure, (e) profile of axial flow velocity in the channel along radial distance at the mid cross-section (i.e. at $z^* = 2.5$ cm), (f) profile of radial substrate deformation along radial distance at the mid cross-section (i.e. at $z^* = 2.5$ cm), (g) surface map of shear strain rate $\left(\frac{\partial v_z^*}{\partial r^*}\right)$ in the channel for the flow rate of 7500 μL/min, and (h) surface map of extensional strain rate $\left(\frac{\partial v_z^*}{\partial z^*}\right)$ in the channel for the flow rate of 7500 μL/min.

Based on detailed theoretical computations for these setups, a couple of key inferences are established. First, the pressure drop over a channel gets reduced as an outcome of the channel's deformation, an effect that is more pronounced for higher flow rates. This finding is in tandem with former microchannel FSI studies[21–23]. Second, the pressure-head developed due to flow through the drainage tube has non-trivial contribution to channel deformation. This is unique to microchannels having walls with graded elasticity, specially with softer outlet than inlet, and is not observed in channels with spatially homogeneous elastic properties[21].

Notes and references

1 L. G. Leal, *Advanced transport phenomena: fluid mechanics and convective transport processes*, Cambridge University Press, 2007, vol. 7.

2 Z. Wang, A. A. Volinsky and N. D. Gallant, *Journal of Applied Polymer Science*, 2014, **131**, 41050.

3 D. E. Hanson, M. Hawley, R. Houlton, K. Chitanvis, P. Rae, E. B. Orler and D. A. Wrobleski, *Polymer*, 2005, **46**, 10989–10995.

4 R. J. Young and P. A. Lovell, *Introduction to polymers*, CRC press, 2011.

5 S.-S. Hsieh and J.-H. Liou, *Biotechnology and Applied Biochemistry*, 2009, **52**, 29–40.

6 Y.-C. Chung, Y.-C. Lin, Y.-L. Hsu, W.-N. T. Chang and M.-Z. Shiu, *Journal of Micromechanics and Microengineering*, 2004, **14**, 1376.

7 Y. Ai, S. W. Joo, Y. Jiang, X. Xuan and S. Qian, *Biomicrofluidics*, 2009, **3**, 022404.

8 X. Xuan and D. Li, *Journal of Micromechanics and Microengineering*, 2005, **16**, 62.

9 A. M. Leshansky, A. Bransky, N. Korin and U. Dinnar, *Physical review letters*, 2007, **98**, 234501.

10 K. Zografos, F. Pimenta, M. Alves and M. Oliveira, *Biomicrofluidics*, 2016, **10**, 043508.

11 Y. Ai, S. Qian, S. Liu and S. W. Joo, *Biomicrofluidics*, 2010, **4**, 013201.

12 C. T. Lu and C. Pan, *Experimental Thermal and Fluid Science*, 2011, **35**, 810–815.

13 T. Cubaud and T. G. Mason, *Physical review letters*, 2006, **96**, 114501.

14 P. Karan, J. Chakraborty and S. Chakraborty, *Electrophoresis*, 2019, **40**, 616–624.

15 S. S. Das, S. Kar, T. Anwar, P. Saha and S. Chakraborty, *Lab on a Chip*, 2018, **18**, 1560–1568.

16 S. S. Das, V. M. Pedireddi, A. Bandopadhyay, P. Saha and S. Chakraborty, *Nano Letters*, 2019, **19**, 7191–7200.

17 S. S. Das, S. Kar, S. Dawn, P. Saha and S. Chakraborty, *Phys. Rev. Applied*, 2019, **12**, 054017.

18 P. Abhimanyu, P. Kaushik, P. K. Mondal and S. Chakraborty, *Journal of Non-Newtonian Fluid Mechanics*, 2016, **231**, 56–67.

19 K. G. Naik, S. Chakraborty and J. Chakraborty, *Soft matter*, 2017, **13**, 6422–6429.

20 P. Karan, J. Chakraborty and S. Chakraborty, *Physics of Fluids*, 2020, **32**, 022002.

21 K. Raj M, J. Chakraborty, S. DasGupta and S. Chakraborty, *Biomicrofluidics*, 2018, **12**, 034116.

22 T. Gervais, J. El-Ali, A. Günther and K. F. Jensen, *Lab on a Chip*, 2006, **6**, 500–507.

23 T. C. Shidhore and I. C. Christov, *Journal of Physics: Condensed Matter*, 2018, **30**, 054002.